A soil–feedstock greenhouse mesocosm matrix for screening carbon dioxide removal via enhanced rock weathering

Dirk Paessler[1], Jens S. Hammes[1,2]*, Ingrid Smet[1], Anna A. Stoeckel[1], Ralf Steffens[1], Jens Hartmann[2], Melissa J. Murphy[1,3]

[1]Carbon Drawdown Initiative, Fürth, Germany

[2]Department of Earth System Sciences, Universität Hamburg, Hamburg, Germany

[3]Mel Murphy Geochemistry, Copenhagen, Denmark

*** Correspondence:** Jens S. Hammes, jens.hammes@carbon-drawdown.de

Keywords: soil–feedstock interaction, ERW, MRV, alkalinity export, machine learning

Abstract

Enhanced rock weathering (ERW) is a carbon dioxide removal (CDR) strategy in which crushed silicate and carbonate rocks are applied to soils to accelerate mineral weathering, releasing base cations and converting CO_2 into dissolved bicarbonate. The ocean is conservatively regarded as the final reservoir for this inorganic carbon. However, mineral dissolution alone does not necessarily translate into CDR. Alkalinity may be neutralised by existing soil acidity, and weathering-derived cations may be retained on soil exchange sites, taken up by plants, incorporated into secondary minerals or leached with non-carbonate anions rather than bicarbonate. Realised CDR is therefore strongly soil-dependent.

In order to test this, here we present the design and methodology of GH2025, a greenhouse mesocosm experiment configured to systematically explore soil–feedstock interactions across a broad parameter space. It follows the multi-year Carbon Drawdown Initiative trial GH2023, which established that soil processes strongly influence alkalinity export and thus CDR, with weathering-derived cations largely retained in exchangeable, carbonate, oxide and clay-mineral pools and strong between-combination variability. These processes complicate the quantification of CDR and the development of robust measurement, reporting and verification (MRV) approaches. Identifying the soil–feedstock combinations that deliver efficient and verifiable CDR therefore remains a central challenge for ERW deployment.

GH2025 comprises 450 lysimeter pots spanning 29 natural, agricultural and engineered technosol soils and 19 feedstocks representing seven mineralogical and dissolution-kinetic categories, including industrial by-products, carbonates, carbonate–silicate mixes and various types of silicates. The design prioritises breadth over replication, using one pot per soil–feedstock combination and three soil-only controls per soil to maximise parameter-space coverage. Leachate is sampled every six to eight weeks and analysed for total alkalinity, dissolved inorganic carbon, electrical conductivity, pH and dissolved oxygen. Following dismantling, soils will be analysed for pH, effective cation exchange capacity, soil inorganic and organic carbon and operationally defined solid-phase cation pools. The resulting dataset will support machine-learning approaches to identify the soil and feedstock properties governing alkalinity export and CDR, and to predict favourable combinations for scalable deployment.

1 Introduction

Enhanced rock weathering (ERW) is a carbon dioxide removal (CDR) strategy that accelerates natural rock weathering by applying finely ground base-rich rocks to soils. During weathering by carbonic acid, mineral dissolution releases base cations and converts CO_2 into dissolved bicarbonate. This bicarbonate can be transported with drainage water and rivers to the ocean, which is conservatively regarded as the final storage reservoir for ERW-derived inorganic carbon (Hartmann et al., 2013; Renforth and Henderson, 2017). However, ERW operates within a complex open environmental system in which mineral dissolution, alkalinity transport and durable inorganic carbon storage do not necessarily occur in the same place or over the same timescales (Schiedung et al., 2026; Suhrhoff et al., 2026).

This complexity is most evident when direct aqueous measurements of alkalinity export are compared with solid-phase estimates of feedstock dissolution or cation release, which can imply substantially greater CDR than is realised as alkalinity export. Although feedstock mineralogy, particle size distribution (PSD) and specific surface area (SSA) influence dissolution kinetics, realised CDR is often lower and more variable than predicted from dissolution kinetics or theoretical CDR potential alone (Brantley, 2025). Alkalinity may be neutralised by existing soil acidity, and weathering-derived cations may be retained on exchange sites, taken up by plants, incorporated into secondary minerals or charge-balanced by non-carbonate anions rather than exported with bicarbonate in drainage water (Vienne et al., 2022; Pogge von Strandmann et al., 2022; Iff et al., 2024; te Pas et al., 2025; Hammes et al., 2025; Maher et al., 2026; Rizzi et al., 2026). Hydrological and geochemical processes in the critical zone can therefore limit alkalinity export (Derry et al., 2026). In this study, we define the system boundary at the base of the lysimeters, where leachate exits the pots. Exported alkalinity therefore represents CDR at the system boundary, but beyond this boundary, it may be stored durably in deeper groundwater or transported to the ocean, transformed or lost during downstream transport; its ultimate contribution to durable CDR depends on these downstream processes (Derry et al., 2026; Isson and West, 2026). Beyond CDR, ERW may also provide agronomic co-benefits through changes in soil chemistry, nutrient availability, crop productivity and yields (Power et al., 2026).

Identifying the soil–feedstock combinations that deliver efficient, detectable and verifiable CDR is therefore a central bottleneck for scaling ERW. Field experiments remain essential for evaluating ERW under real deployment conditions, but they are expensive, heterogeneous and poorly suited to testing large numbers of soil–feedstock combinations. Soil mesocosm studies bridge this gap by enabling systematic testing of a wider range of soil–feedstock combinations under controlled conditions, while allowing for more complete mass-balance accounting than is possible in field trials. However, published ERW mesocosm and pot trials typically only span weeks to months (e.g., ten Berge et al., 2012; Amann et al., 2020; Kelland et al., 2020; Vienne et al., 2022; te Pas et al., 2023; Rizzi et al., 2026).

Our earlier Carbon Drawdown Initiative two-year greenhouse mesocosm trial GH2023 compared multiple soil–feedstock combinations under replicated conditions (Hammes et al., 2025). Leachate alkalinity export was strongly soil-dependent: the same feedstock could increase or decrease alkalinity export relative to an untreated control depending on the soil to which it was applied. Acidic soils with low effective cation exchange capacity (CEC_{eff}) and negligible carbonate background generally showed the clearest alkalinity export, whereas neutral-to-alkaline, carbonate-bearing soils showed weak or negative responses. After an initial pot-settling phase, consistent relationships emerged between total alkalinity (TA), electrical conductivity (EC) and major cations in leachate.

Stronger coupling was observed for more reactive feedstocks characterised by faster expected dissolution kinetics, as weathering products were increasingly mobilised into solution. The study also showed that over the experiment time of 24 months, weathering-derived cations were more often retained in solid-phase exchangeable, carbonate, oxide and clay-mineral fractions than exported as alkalinity in leachate (Hammes et al., 2025).

Together these findings demonstrated that the soil matrix can act as a dominant near-term sink for weathering products, some of which may subsequently be remobilised, and that ERW performance must be evaluated with complementary aqueous and solid-phase measurements. Whilst GH2023 showed soil-dependent responses in some cases, the underlying processes could not always be identified and are likely to vary amongst soils. This motivated GH2025, which shifts the emphasis from a deeper, more replicated design towards a broader screening across a wider soil–feedstock matrix.

GH2025 is a 450-pot lysimeter experiment spanning 29 soils and 19 feedstocks, configured to maximise the dimensionality of the soil–feedstock parameter space. The soils encompass broad physicochemical gradients in pH, CEC_{eff}, clay content, soil inorganic carbon (SIC) and soil organic carbon (SOC). The feedstocks represent seven categories based on mineralogical dissolution kinetics: industrial by-products, carbonates, carbonate–silicate mixes, Ca-(Mg-)silicates, ultramafic, mafic and felsic silicates. Selected feedstocks are included as milled–unmilled pairs. Each soil–feedstock combination is represented by a single treatment pot, with three soil-only controls per soil. This design deliberately prioritises breadth over within-combination replication.

To evaluate how mineral dissolution translates into measurable carbon removal, GH2025 combines aqueous- and solid-phase measurements with sensor data. Leachate is sampled every six to eight weeks for volume, pH, EC, dissolved oxygen, TA and dissolved inorganic carbon (DIC). At the end of the experiment, soils will be analysed for changes in SIC, SOC and solid-phase cation pools, allowing alkalinity export to be distinguished from cation mobilisation and retention, and other forms of solid-phase carbon storage to be assessed. With a planned runtime of approximately two years and one pot per soil–feedstock combination, GH2025 will be unusually long-running and broad for an ERW mesocosm study. Its multidimensional dataset is intended to support subsequent data-driven analysis of the processes governing CDR across diverse soil–feedstock combinations, improving predictive understanding of ERW performance and informing future MRV (measurement, reporting and verification) approaches for commercial deployment. GH2025 was established in phases, and at the time of writing the experiments are still ongoing.

Models are increasingly viewed as a means of extrapolating observations from intensively monitored field sites across heterogeneous deployment areas, thereby reducing MRV costs and helping to identify the locations and soil–feedstock combinations in which ERW is most likely to be effective (Kukla and Chay, 2026; Isometric, 2026). Process-based, data-driven and hybrid approaches provide different but complementary insights into the factors governing CDR. GH2025 is designed to support this development by generating a standardised, high-dimensional dataset spanning diverse soils and feedstocks. Rather than estimating a precise annual CDR rate for each individual combination, subsequent modelling will use machine-learning methods to identify the properties and processes controlling alkalinity generation, cation mobilisation and retention. These approaches can capture non-linear relationships and interactions among predictors, allowing us to assess how well ERW performance can be predicted using routinely available soil and feedstock characterisation data.

2 Materials and Equipment

2.1 Experimental setup

GH2025 builds on the greenhouse mesocosm design described in detail by Hammes et al. (2025). Each mesocosm comprises an upper lysimeter containing the soil column, feedstock amendment and vegetation, which drains into a lower leachate collection tank (Figure 1). To maintain continuity with the earlier Carbon Drawdown Initiative GH2023 trial and to allow comparison between experimental generations, the lysimeter architecture was retained with only minor modifications: the drainage interface was improved, feedstock was homogenised throughout the full ~ 20 cm soil column, and the single-species *Lolium perenne* cover was replaced with a grass–legume mixture comprising, by seed mass, 40% *Festuca arundinacea*, 30% *Lolium perenne* subsp. *perenne* and 30% *Trifolium repens* 'Microclover', supplemented with *Agrostis capillaris* and *A. canina* in strongly acidic soils and technosols. Greenhouse operating conditions were warmer and less humid than outside ambient conditions, with a median daily air temperature of ~21–22 °C, and with irrigation rates of ~2,000 to 4,000 mm yr-1 to maintain leachate generation. Further experimental and operational details are provided in Supplementary Section S1 and in Hammes et al. (2025).

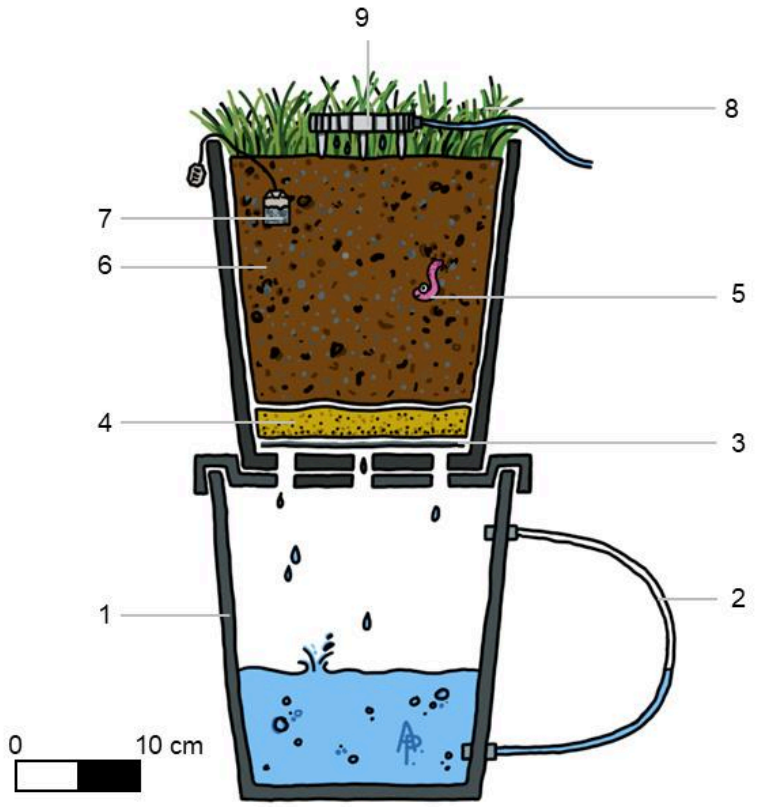

Figure 1. Schematic of the greenhouse mesocosm lysimeter design used in GH2025, modified after Hammes et al. (2025). Each mesocosm comprises an upper vegetated soil–feedstock column that

drains into a lower leachate collection tank, enabling repeated leachate sampling under controlled greenhouse conditions.

2.2 Soils

The 29 soils were selected to span wide gradients in physicochemical properties expected to exert first-order control on CDR. These soils comprise natural and agricultural soils from temperate regions, as well as engineered technosols. The natural and agricultural soils were collected by removing the uppermost ~5 cm of organic-rich surface material and sampling the underlying soil to a depth of approximately 20 cm. Pure quartz filter sand and organic-rich material (Bavarian Black Swamp, BBS) were used to construct selected technosols and as an additional treatment on the acidic Wolfland soil to widen the range of soil properties represented. An additional batch of LUFA 2.2, a reference soil from the LUFA Speyer series used in GH2023, was included as LUFA 2.2 C for the vegetation bridge sub-experiment linking GH2023 to GH2025 (see Experimental design in Section 3.1). Soil preparation, homogenisation and archiving are described in Supplementary Section S2.

Soil pH and EC were determined in-house at the CDI laboratory. CEC_{eff}, base saturation and exchangeable acidity were determined at the Soil Laboratory of the Institute of Geography, Friedrich-Alexander University Erlangen-Nuremberg, Germany (FAU). Soil organic carbon and total nitrogen were determined by dry combustion at the Thünen Institute, Germany. $\delta^{13}C$ was measured by elemental analyser-isotope ratio mass spectrometry (EA-IRMS) to screen the soils for the presence of inorganic carbon. For carbonate-containing soils, acid fumigation following Harris et al. (2001) was used to remove inorganic carbon prior to SOC determination. Total carbon was measured separately by dry combustion, and SIC was determined by difference. Bulk major- and selected trace-element composition were determined by X-ray fluorescence (XRF) and quantitative mineralogy by X-ray diffraction (XRD) at Qmineral (Leuven, Belgium). Soil physicochemical parameters are reported in Table 1; exchangeable-cation composition, bulk soil geochemistry and full quantitative mineralogy are provided in Supplementary Tables S1–S3. Soil grain size by wet sieving and SediGraph are presented in Supplementary Tables S4. Analytical methods are summarised in Table S5.

Soil textures were determined by wet sieving and high-resolution X-ray SediGraph analysis at FAU. Soil textures span USDA classes from sand to silty clay loam, with wide variation in sand (8.96–91.78%), silt (2.64–65.17%) and clay (4.76–36.96%) content. Soil pH (0.01 M $CaCl_2$) ranges from strongly acidic to slightly alkaline (3.34–7.50). Several soils with pH < 4 fall outside the range typical of managed agricultural land and were included as acidic end-members, while the calcareous soil Fabrikfeld represents the carbonate-rich end-member in our setup. Effective CEC ranges from 1.1 to 25.4 cmol kg^{-1}, SOC from 0.06 to 4.50% and SIC from below detection limit to 6.80%. Base saturation exceeds 97% in most soils but declines sharply below ~pH 4.5, reaching ~29%, ~35%, and ~52% in Pod 12,Wolfland and Pod 12 MIR, respectively. Ca^{2+} is the dominant exchangeable cation, comprising ~59–94% of the exchange complex in the less acidic soils, but only ~14–31% in the three most acidic soils, where exchangeable acidity accounts for ~48–68% of the CEC_{eff}. Exchangeable acidity is highest in Wolfland (pH 3.34) and Pod 12 (pH 3.68). Total nitrogen (0.02–0.31%) is strongly positively correlated with organic-matter content.

Bulk soil mineralogy is dominated by quartz (ranging from 41.9–88.5%), undifferentiated 2:1 layer silicates (2.2–43.5%) and feldspars (plagioclase up to 13.8% and K-feldspar 1.5–15.7%). Mineralogical end-members include Fabrikfeld, which contains ~79% calcite; Pruem, with ~44% 2:1 layer silicates; Marsianer, a strongly weathered Fe-oxide-bearing soil (containing goethite, hematite

and ~86% quartz); and Kirchweg and Alkener Berg, which contain ~15–16% K-feldspar. Results from GH2023 indicated that, under the elevated temperatures and irrigation rates used in the greenhouse, weathering of native soil K-feldspars contributed to K^+ in the leachate, highlighting the need to distinguish soil-derived cation release from feedstock-derived weathering signals (Hammes et al., 2025).

Based on measured topsoil properties, including pH, texture, CEC_{eff}, and soil mineralogy, the GH2025 soils most closely resemble temperate agricultural Cambisols and Luvisols. This comparison is indicative rather than a formal pedon-level classification, which would require diagnostic profile and horizon data not collected for these soils (IUSS Working Group WRB, 2022). Together, these Reference Soil Groups cover approximately 15% of the global land area and are among those most widely used for agriculture (FAO and ITPS, 2015). They also cover over 40% of the EU's land area (Jones et al., 2005), making them broadly representative of European agricultural soils. Due to logistical constraints on sourcing international soils, several other globally relevant agricultural soil groups are not represented, including highly weathered, kaolinite- and Fe-oxide-dominated soils of the humid tropics, such as Ferralsols and Acrisols; smectite-rich Vertisols; dark, organic-rich Chernozems; volcanic Andosols; and the calcareous, saline or sodic soils typical of arid regions.

2.3 Feedstocks

Nineteen materials were selected to span broad variation in composition, theoretical maximum CDR potential (E_{pot}) and expected dissolution kinetics. Each feedstock was characterised for bulk major- and selected trace-element composition by XRF and for quantitative mineralogy by XRD, as well as for particle size distribution by wet laser diffraction and specific surface area using the BET method at Qmineral (Leuven, Belgium). CDR-relevant mineralogy, particle size distribution and BET specific surface area are summarised in Tables 2 and 3. Analytical methods are summarised in Table S5. Full bulk geochemistry, quantitative mineralogy and particle size distributions are provided in Supplementary Tables S6–S8, respectively. The theoretical maximum CDR potential (E_{pot}) of each feedstock was calculated from XRF-derived major element composition (Steinour, 1959; Renforth, 2019). Calculated E_{pot} values for the feedstocks ranged from 253 to 1,244 kg CO_2 t^{-1}. E_{pot} can, however, overestimate CDR potential where base cations are hosted in relatively less reactive mineral phases and are not released on CDR-relevant timescales, or where carbonate-hosted cations are not distinguished from silicate-hosted cations (Power et al., 2025). We therefore also calculated a carbonate-corrected theoretical maximum CDR potential (Max CDR_{pot}) using quantitative XRD mineralogy to identify and correct for cations hosted in carbonate phases. Both E_{pot} and Max CDR_{pot} are reported in Supplementary Table S6. The equations, assumptions and full derivation are provided in Supplementary Section S4.

The main CDR-relevant base-cation-bearing silicates, carbonates, oxides and hydroxides span several orders of magnitude in dissolution rates (Palandri and Kharaka, 2004; Heřmanská et al., 2022, 2023; Oelkers and Addassi, 2025; Figure 2).

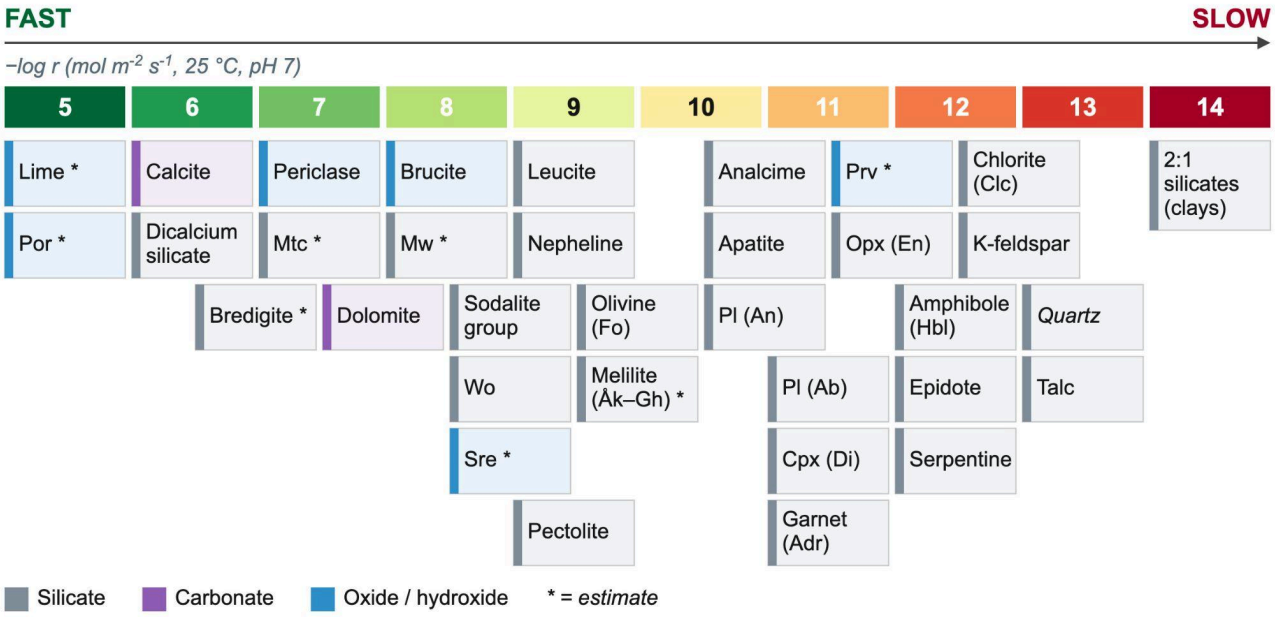

Figure 2. GH2025 feedstock minerals grouped by expected dissolution rate at 25 °C and pH 7, expressed as BET-surface-area–normalised, far-from-equilibrium −log r (mol m^{-2} s^{-1}) from published rate-law parameters (Palandri and Kharaka, 2004) and the internally consistent databases of Heřmanská et al. (2022, 2023) and Oelkers and Addassi (2025). Asterisks denote minerals for which rates were estimated from a chemical analogue or single literature source. Quartz is shown as a non-base-cation releasing reference; apatite releases Ca^{2+} but is a phosphate mineral. Mineral abbreviations: Cpx, clinopyroxene; Mtc, monticellite; Mw, merwinite; Opx, orthopyroxene; Pl, plagioclase; Por, portlandite; Prv, perovskite; Sre, srebrodolskite; Wo, wollastonite. End-member abbreviations: Ab, albite; Adr, andradite; An, anorthite; Clc, clinochlore; Di, diopside; En, enstatite; Fo, forsterite; Hbl, hornblende; Åk–Gh, åkermanite–gehlenite.

Based on their CDR-relevant mineralogy, the 19 feedstocks were assigned to seven categories ordered by inferred dissolution kinetics, from fastest to slowest dissolving (Table 2): (1) *Industrial by-products* — one steel slag rich in industrially formed Ca-oxides, Ca-hydroxides and dicalcium silicates; (2) *Carbonates* — two natural limestones (BB limestone, MK limestone) composed almost entirely of fast-dissolving carbonate minerals; (3) *Carbonate–silicate mixes* — three materials containing 12–50% carbonate alongside silicate assemblages spanning a range of dissolution rates: Angryd Frankenstein, an ultrafine dust generated during the milling of multiple feedstocks and recovered from the filtration system; a 50/50 blend of MK limestone and VV peridotite; and a metabasalt; (4) *Ca-(Mg-)silicates* — four materials dominated by fast-dissolving Ca- and Mg-silicates, two synthetic materials (Calcio-olivine, Monticellite), which also contain reactive periclase, and two natural skarn assemblages (Monticellite skarn, Wollastonite skarn); (5) *Ultramafic silicates* — two relatively unaltered mantle rocks with > 70 wt% olivine (Peridotite, VV peridotite); (6) *Mafic silicates* — five natural mafic volcanic rocks, comprising one basanite (‘Eifelgold’ basanite), one basalt (DP basalt) and three nephelinites (BD nephelinite, KL nephelinite, TC nephelinite); and (7) *Felsic silicates* — two ultrafine glacial rock flours with the slowest-dissolving mineral assemblages (Glacial rock flour, Glacial power flour).

Reactivity is governed not only by mineralogy, but also by PSD and SSA, which influence the reactive surface area exposed to weathering. Laboratory-derived dissolution rates commonly exceed

rates observed under field conditions by several orders of magnitude. This discrepancy reflects multiple interacting factors, including differences in reactive surface area, solution chemistry and saturation state, hydrological transport, spatial and temporal heterogeneity, and biological activity (Brantley, 2025). To test the influence of grain size on feedstock reactivity, several feedstocks were included in both their original 'as-received' (O) and milled (M) forms, allowing comparison between materials with the same bulk mineralogy but contrasting PSD and SSA.

Selected feedstocks were milled in a DemiNo® 2250 impact mill (*Prallstrommühle*; Aufbereitungstechnologie NOLL GmbH, Bobingen, Germany), which combines pin-mill and air-whirl classification in a single pass. Original 'as-received' feedstocks spanned d_{50} values of 1.6–213.0 µm and d_{90} values of 3.8–448.7 µm, whereas the milled variants were finer and less variable in particle size (d_{50} 5.3–22.6 µm; d_{90} 12.9–45.7 µm). BET specific surface area ranged from 0.1 to 19.2 $m^2 g^{-1}$ across all feedstock variants. The two glacial rock flours are finer than the milled feedstocks (d_{50} 1.6–2.4 µm, d_{90} 3.8–5.2 µm, BET 16.4–17.8 $m^2 g^{-1}$). Angryd Frankenstein, an ultrafine filter dust generated during the milling of the other feedstocks, was also included as an additional fine-grained comparison (d_{50} 2.0 µm, d_{90} 3.9 µm, BET 16.5 $m^2 g^{-1}$).

3 Methods

3.1 Experimental design

GH2025 is structured in four complementary experimental tiers incorporating 29 soils and 19 feedstocks spanning broad variation in physicochemical properties, feedstock composition, expected reactivity and particle size. The design prioritises breadth across the soil–feedstock interaction space generating a standardised dataset for machine-learning approaches (Figure 3, Supplementary Table S9). These analyses will help to identify the principal controls on alkalinity generation and export, cation mobilisation and retention and ultimately CDR, as well as how well ERW performance and favourable soil–feedstock combinations can be predicted from routinely available soil and feedstock properties.

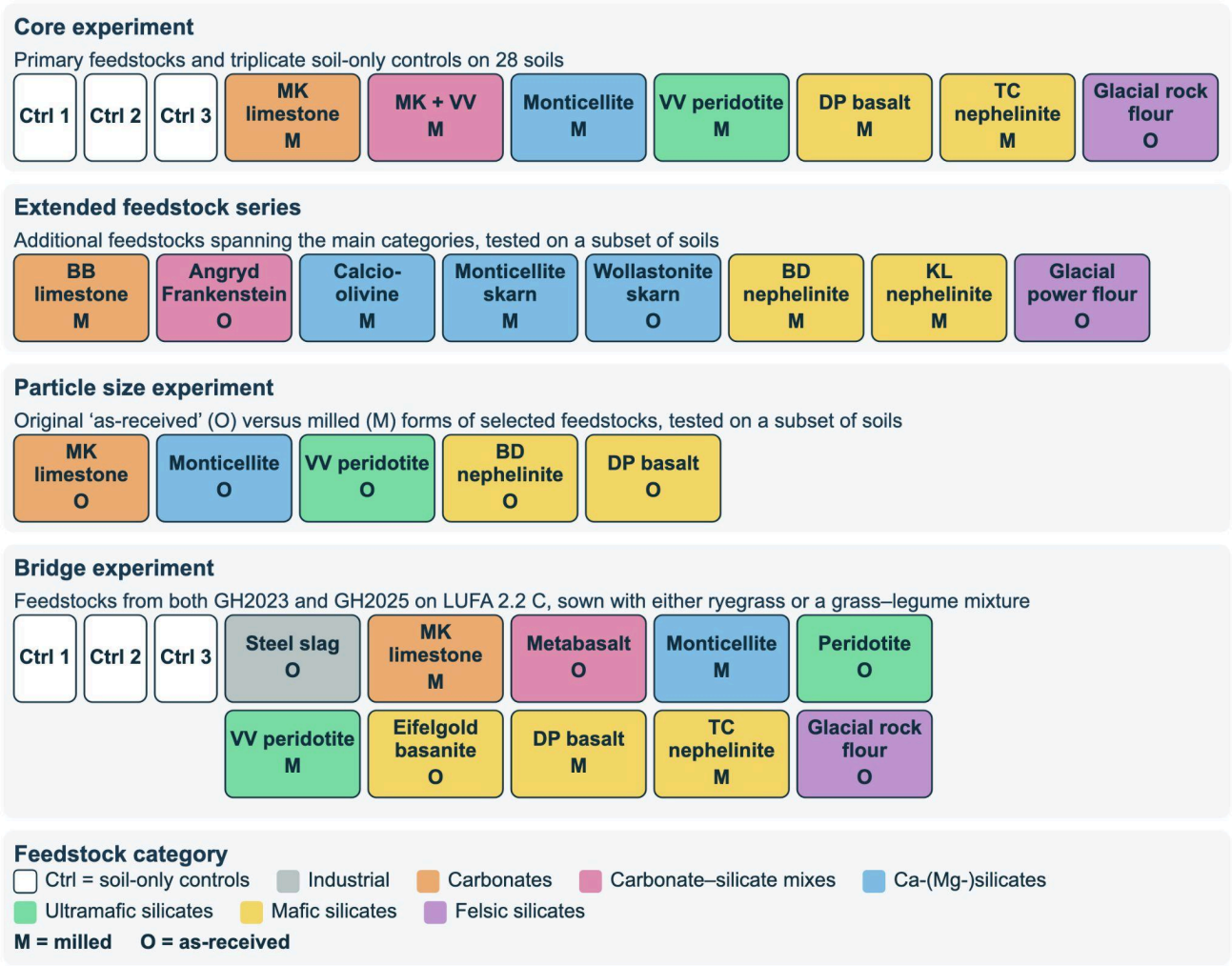

Figure 3. Overview of the GH2025 experimental design: a core experiment, an extended feedstock series, an original 'as-received' (O) versus milled (M) particle size comparison, and a bridge experiment linking GH2023 and GH2025. The complete set of soil–feedstock combinations is presented in Supplementary Table S9.

The *core experiment* provides a common screening backbone across 28 soils. Each soil is represented by three soil-only controls and seven primary feedstock treatments (10 pots per soil). The core feedstocks span the main categories described in Section 2.3, ordered by inferred dissolution kinetics from fastest to slowest dissolving: carbonates, carbonate–silicate mixes, Ca-(Mg-)silicates, and ultramafic, mafic and felsic silicates. Mafic volcanic rocks, among the feedstocks most commonly used for ERW, are represented by both a silica-undersaturated nephelinite (TC nephelinite) and a silica-saturated tholeiitic basalt (DP basalt). The carbonate feedstock is a dolomite-bearing limestone (MK limestone).

The *extended feedstock series* broadens the geochemical and mineralogical diversity of the design by adding eight additional feedstocks to 13 of the core 28 soils: one high-purity calcitic limestone (BB limestone), one carbonate–silicate mix, three Ca-(Mg-)silicates, two mafic silicates, and one additional ultrafine glacial rock flour.

The *particle size experiment* isolates the effect of physical processing, specifically PSD and SSA, from that of bulk mineralogy. For six soils included in both the core and extended series, the original 'as-received' (O) variants of five feedstocks were applied alongside their corresponding milled (M) variants. Together, the paired feedstocks represent the carbonate, Ca-(Mg-)silicate, ultramafic and mafic silicate categories.

The *bridge experiment* links GH2023 to GH2025 using a standardised agricultural reference soil and feedstocks common to both trials, while isolating the effect of the change in vegetation within GH2025. A new batch of LUFA 2.2 (batch C) was used to establish two matched 13-pot sets, each comprising three soil-only controls and ten single-pot feedstock treatments representing four GH2023 feedstocks and six GH2025 feedstocks. One set was sown with the GH2023 *Lolium perenne* monoculture and the other with the GH2025 grass–legume mixture. Because the soil, feedstock treatments and experimental conditions were held constant between the two sets, differences between them can be interpreted as an effect of the vegetation treatment.

A further ten pots fall outside of these four experiments: four additional treatments on Wolfland, the most acidic and sandiest soil (pH 3.34), blended with BBS to increase its organic carbon content, and six additional soil–feedstock combinations related to collaborative ERW field projects.

3.2 Leachate monitoring

Leachate is collected from each mesocosm every six to eight weeks and measured for volume, pH, EC, dissolved oxygen, temperature, TA and sampled for DIC. During selected sampling rounds cations and anions are analysed. Methods and instruments are summarised in Supplementary Table S5; full protocols are given in Supplementary Section S3 and Hammes et al. (2025).

3.3 Design rationale: prioritising variation over replication

GH2025 prioritises breadth across the soil–feedstock parameter space over replication within any one combination. Each soil–feedstock treatment is represented by one mesocosm, with triplicate soil-only controls per soil. This decision was informed by GH2023, in which some soil–feedstock combinations produced significant increases in TA. However, differences between combinations generally exceeded within-treatment variability and measurement uncertainty in leachate TA, EC and pH (Hammes et al., 2025). Thus, broadening the parameter space is more informative than replicating a narrow set of combinations. For predictive modelling, this wider coverage reduces the uncertainty across the parameter space by exposing the model to a broader range of soil and feedstock properties and their interactions, whereas additional replication primarily refines uncertainty around combinations already represented. This approach substantially expands the number of combinations that can be tested within the available greenhouse capacity; full replication of the matrix would require several thousand pots and was not operationally feasible.

Although individual treatment combinations are unreplicated, each feedstock is evaluated across multiple soils. This enables its consistency and soil dependence to be assessed across the wider dataset and allows anomalous pots to be identified against broader response patterns, although it does not provide a direct estimate of within-treatment variability.

3.4 Data quality control

Data quality procedures combine operational records with comparisons of time-series leachate and sensor data to identify disturbances affecting individual pots or sampling periods. Irrigation

inconsistencies due to blocked drainage, incomplete leachate recovery, pest-control applications and other pot-level interventions are recorded throughout the experiment. Abrupt changes or inconsistencies relative to preceding measurements in leachate volume, pH, EC and TA are flagged and evaluated against analytical uncertainty of the relevant measurement and subsequent time-series data. Based on the stabilisation period observed in GH2023, early measurements are treated separately because soil settling, establishment of drainage pathways and initial flushing of soluble native salts can produce transient responses unrelated to longer-term feedstock weathering.

3.5 Post-experiment characterisation

At the end of the experiment, the mesocosms will be dismantled and the soils sampled to assess changes in physicochemical and solid-phase properties to be assessed over the experimental period and determine the fate of weathering-derived cations. The majority of the initial soil-characterisation suite of parameters will be repeated, including pH, EC, CEC_{eff}, base saturation, exchangeable acidity, SIC, SOC and total nitrogen. Bulk geochemistry and quantitative mineralogy will be reassessed for selected pots where geochemical and mineralogical changes are expected to be detectable.

Depending on available resources, we may use sequential extractions to quantify cations held in operationally-defined exchangeable, carbonate-associated, oxide-associated and clay-mineral or residual fractions (e.g., Hammes et al., 2025), alongside solid-phase cation mass-balance approaches including SOMBA (Suhrhoff et al., 2025) and total cation accounting (TCA; Baum et al., 2024) to trace the fate of weathering-derived cations and estimate feedstock dissolution.

SEM imaging and elemental mapping of the recovered feedstock "tea-bag" sachets could be used to assess changes in mineralogy, grain morphology and specific surface area, including evidence for preferential dissolution, surface passivation and secondary mineral neoformation, and associations between potentially toxic elements and specific mineral phases. These observations will also enable evaluation of shrinking-grain/core and reactive-surface-area assumptions used in process-based models.

Together, leachate chemistry and solid-phase measurements provide complementary evidence for tracing the mobilisation and retention of weathering-derived cations and determining how feedstock dissolution translates into alkalinity export and ultimately CDR.

4 Anticipated Results

GH2025 is designed to reconcile the mass balance between mineral dissolution, cation retention and exported alkalinity, a key unresolved challenge for ERW monitoring, reporting and verification (Schiedung et al., 2026). By tracing weathering-derived cations and carbon across leachate and soil pools, the experiment will help characterise time lags between feedstock dissolution, cation mobilisation and alkalinity export, and explain why feedstock dissolution does not necessarily translate directly into quantifiable CDR.

The primary output will be a standardised, model-ready dataset that links initial soil and feedstock properties to time-resolved leachate chemistry and end-of-experiment changes in soil properties across the experimental matrix. We intend to use machine-learning approaches to test whether alkalinity export and CDR performance can be predicted from routinely available soil and feedstock properties. Model performance will be evaluated using withheld soil–feedstock combinations and feedstocks and soils independently excluded, thereby testing its ability to generalise new pairings of characterised materials and to previously unseen feedstocks and soils. The modelling will also be

used to assess whether measurements such as leachate EC, TA and drainage volume, can reduce reliance on more resource-intensive monitoring and lower the overall MRV burden for ERW.

5 Conclusions

GH2025 provides a standardised experimental framework for examining ERW across a broad range of temperate soils and feedstocks representing seven mineralogical and dissolution kinetic categories, from rapidly reacting industrial by-products, carbonates, carbonate–silicate mixes and Ca-(Mg-)silicates to slower-weathering ultramafic, mafic and felsic silicates. While the present dataset is constrained to these soil–feedstock combinations, the experimental, analytical and modelling framework is intended to be extended to other soil regions, climates and feedstock types as further data becomes available.

GH2025 is designed as a screening framework rather than to provide definitive carbon-removal estimates for every soil–feedstock combination. By coupling time-resolved leachate chemistry with post-experiment solid-phase characterisation, GH2025 is designed to determine how feedstock weathering translates into cation mobilisation and retention within soil, alkalinity generation and export and measurable CDR. The resulting model-ready dataset is intended to support data-driven approaches, including machine learning, to identify the soil and feedstock properties associated with effective and detectable CDR, and to assess whether routinely available characterisation data and lower-cost measurements can guide soil–feedstock selection and reduce MRV costs.

6 Conflict of Interest

DP is the CEO, owner and sole funder of CDI and is an investor in several carbon dioxide removal companies. He also holds three patents related to enhanced weathering that are unrelated to the methods or findings presented here. MJM was formerly an employee at UNDO and retains homeopathically minor stock options in the company. No CDI-affiliated author holds an advisory or board position in any company that supplied materials for the study. The remaining authors declare no commercial or financial relationships that could be construed as a potential conflict of interest.

7 Author Contributions

DP, RS, JH, JSH, IS and AAS conceived and designed the experiment; AAS, JSH, RS and IS conducted the experimental and laboratory analyses; JSH, DP, RS, IS, AAS and MJM performed the formal data analysis. DP provided funding and developed the data processing pipeline. MJM and JSH prepared the original draft. All authors reviewed and edited the manuscript and approved the submitted version.

8 Funding

This research was funded entirely by the Carbon Drawdown Initiative (CDI).

9 Acknowledgments

The authors gratefully acknowledge everyone who contributed to the establishment and ongoing operation and maintenance of the greenhouse experiment. We also warmly thank all our many collaborators across the Carbon Drawdown Initiative community, whose collective support and contributions have made GH2025 possible. We especially wish to thank Marcus Schiedung at the Thünen Institute, Germany, for running the SOC/SIC analyses.

Generative AI tools were used during manuscript preparation to support iterative drafting, restructuring and language editing, and to assist in the preparation of schematic figures. The authors used ChatGPT and Claude. All AI-assisted text and visual content was critically reviewed, revised and verified by the authors for scientific accuracy. The authors take full responsibility for the final manuscript and figures.

A preprint version of this manuscript has been deposited in the CDRXIV repository (DOI: [insert DOI]).

10 Supplementary Material

The Supplementary Material for this article is provided as a separate file and comprises Supplementary Sections S1–S4 (extended experimental setup, soil preparation, detailed analytical protocols, and the carbonate-corrected CDR-potential derivation) and Supplementary Tables S1–S10.

11 Data Availability Statement

The original contributions presented in the study are included in the article/supplementary material, further inquiries can be directed to the corresponding author/s. The data can also be found at Github: https://github.com/dirkpaessler/carbdown_greenhouse_experiment_2025 and archived for citation via Zenodo: doi.org/10.5281/zenodo.23798190.

12 References

Amann, T., Hartmann, J., Struyf, E., de Oliveira Garcia, W., Fischer, E. K., Janssens, I. A., et al. (2020). Enhanced weathering and related element fluxes – a cropland mesocosm approach. Biogeosciences 17, 103–119. doi: 10.5194/bg-17-103-2020

Baum, M., Liu, H., Schacht, L., Schneider, J. and Yap, M. (2024) 'Mass-balance MRV for carbon dioxide removal by enhanced rock weathering: Methods, simulation, and inference', arXiv preprint arXiv:2407.01949. doi: 10.48550/arXiv.2407.01949

Derry, L. A., Maher, K., and Chadwick, O. A. (2026). Critical zone processes limit alkalinity export from natural basaltic systems. Nature 657, 150–155. doi: 10.1038/s41586-026-10936-3

Hammes, J. S., Hartmann, J., Barth, J. A. C., Linke, T., Smet, I., Hagens, M., et al. (2025). Soil processes govern alkalinity and cation retention in enhanced weathering for carbon dioxide removal. EGUsphere [preprint]. doi: 10.5194/egusphere-2025-5402

Harris, D., Horŵath, W.R., van Kessel, C., 2001. Acid fumigation of soils to remove carbonates prior to total organic carbon or CARBON-13 isotopic analysis. Soil Sci. Soc. Am. J. 65, 1853–1856. https://doi.org/10.2136/sssaj2001.1853

Hartmann, J., West, A. J., Renforth, P., Köhler, P., De La Rocha, C. L., Wolf-Gladrow, D. A., et al. (2013). Enhanced chemical weathering as a geoengineering strategy to reduce atmospheric carbon dioxide, supply nutrients, and mitigate ocean acidification. Rev. Geophys. 51, 113–149. doi: 10.1002/rog.20004

Heřmanská, M., Voigt, M. J., Marieni, C., Declercq, J., and Oelkers, E. H. (2022). A comprehensive and internally consistent mineral dissolution rate database: Part I. Primary silicate minerals and glasses. Chem. Geol. 597, 120807. doi: 10.1016/j.chemgeo.2022.120807

Heřmanská, M., Voigt, M. J., Marieni, C., Declercq, J., and Oelkers, E. H. (2023). A comprehensive and internally consistent mineral dissolution rate database: Part II. Secondary silicate minerals. Chem. Geol. 636, 121632. doi: 10.1016/j.chemgeo.2023.121632

Iff, N., Renforth, P., and Pogge von Strandmann, P. A. E. (2024). The dissolution of olivine added to soil at 32°C: the fate of weathering products and its implications for enhanced weathering at different temperatures. Front. Clim. 6, 1252210. doi: 10.3389/fclim.2024.1252210

International Organization for Standardization (ISO) (2025). Environmental solid matrices - Determination of the specific electrical conductivity. ISO 11265:2025, 2nd Edn. Geneva: ISO.

Isometric (2026). Model and Measurement Based Quantification of Enhanced Weathering. Version 1.0. Available online at: https://registry.isometric.com/module/model-quantification-enhanced-weathering/1.0 (accessed September 1, 2026).

Isson, T. T., and West, A. J. (2026). Can enhanced alkalinity store carbon durably? Science 392, 808–810. doi: 10.1126/science.adz2620

IUSS Working Group WRB (2022). World Reference Base for Soil Resources 2022 – International Soil Classification System for Naming Soils and Creating Legends for Soil Maps. Vienna: International Union of Soil Sciences.

Jones, A., Montanarella, L., and Jones, R. J. A. (Eds.) (2005). Soil Atlas of Europe. Luxembourg: European Soil Bureau Network, European Commission.

Kelland, M. E., Wade, P. W., Lewis, A. L., Taylor, L. L., Sarkar, B., Andrews, M. G., et al. (2020). Increased yield and CO_2 sequestration potential with the C_4 cereal Sorghum bicolor cultivated in basaltic rock dust-amended agricultural soil. Glob. Change Biol. 26, 3658–3676. doi: 10.1111/gcb.15089

Kukla, T., and Chay, F. (2026). The role of reactive transport models in enhanced weathering today. CarbonPlan. Available online at: https://carbonplan.org/research/modeling-bytes-01-primer (accessed September 1, 2026)

Maher K, Rogers B, Perzan Z, Kukla T. (2026). Surface Proton Reservoirs Constrain Alkalinity Export from Enhanced Weathering. Environ. Sci. Technol. 60(34):24044-24056. doi: 10.1021/acs.est.6c03236.

Oelkers, E. H., and Addassi, M. (2025). Kinec_v3: a computer database for the calculation of the dissolution rates of the major rock-forming minerals. Chem. Geol. 695, 123041. doi: 10.1016/j.chemgeo.2025.123041

Paessler, D., Hammes, J. S., Smet, I., Stoeckel, A. A., Steffens, R., Hartmann, J., and Murphy, M. J. (2026). A soil–feedstock greenhouse mesocosm matrix for screening carbon dioxide removal via enhanced rock weathering. CDRXIV [Preprint]. doi: [insert DOI].

Palandri, J. L., and Kharaka, Y. K. (2004). A Compilation of Rate Parameters of Water–Mineral Interaction Kinetics for Application to Geochemical Modeling. US Geological Survey Open-File Report 2004-1068. Menlo Park, CA: US Geological Survey. doi: 10.3133/ofr20041068

Pogge von Strandmann, P. A. E., Tooley, C., Mulders, J. J. P. A., and Renforth, P. (2022b). The dissolution of olivine added to soil at 4°C: implications for enhanced weathering in cold regions. Front. Clim. 4, 827698. doi: 10.3389/fclim.2022.827698

Power, I.M., Hatten, V.N.J., Guo, M., Schaffer, Z.R., Rausis, K., and Klyn-Hesselink, H. (2025). Are enhanced rock weathering rates overestimated? A few geochemical and mineralogical pitfalls. Frontiers in Climate 6:1510747. doi: 10.3389/fclim.2024.1510747

Power, I. M., Spence, J., Guo, M., Wilson, S., & Watmough, S. (2026). Enhanced rock weathering has greater promise as a sustainable farming practice than a CO2 removal technology. Proc. Natl. Acad. Sci. U.S.A. 123, e2602421123. doi: 10.1073/pnas.2602421123

Renforth, P., and Henderson, G. (2017). Assessing ocean alkalinity for carbon sequestration. Rev. Geophys. 55, 636–674. doi: 10.1002/2016RG000533

Renforth, P. (2019). The negative emission potential of alkaline materials. Nature Communications 10, 1401. doi: 10.1038/s41467-019-09475-5

Rizzi M, Chang E and Pallud C (2026) Evidence for temporal decoupling of olivine weathering and inorganic carbon removal in unsaturated soil columns. Front. Clim. 8:1964775. doi: 10.3389/fclim.2026.1964775

Steinour, H.H. (1959). Some effects of carbon dioxide on mortars and concrete – discussion. Journal of the American Concrete Institute 30, 905–907

Schiedung, M., Harrington, K. J., Dupla, X., et al. (2026). Uncertainties of enhanced rock weathering for climate-change mitigation. Nat. Rev. Earth Environ. 7, 253–266. doi: 10.1038/s43017-026-00761-7

Suhrhoff, T. J., Reershemius, T., Jordan, J. S., Li, S., Zhang, S., Milliken, E., et al. (2025). An updated framework and signal-to-noise analysis of soil mass balance approaches for quantifying enhanced weathering on managed lands. Environ. Sci. Technol. 59, 26440–26453. doi: 10.1021/acs.est.5c08303

Suhrhoff, T. J., Dietzen, C., Kukla, T., et al. (2026). An ecosystem of carbon dioxide removal reviews – Part 3: enhanced weathering. CDRXIV[preprint]. doi: 10.70212/cdrxiv.preprint.417

te Pas, E. E. E. M., Hagens, M., and Comans, R. N. J. (2023). Assessment of the enhanced weathering potential of different silicate minerals to improve soil quality and sequester CO_2. Front. Clim. 4, 954064. doi: 10.3389/fclim.2022.954064

te Pas, E. E. E. M., Chang, E., Marklein, A. R., Comans, R. N. J., and Hagens, M. (2025). Accounting for retarded weathering products in comparing methods for quantifying carbon dioxide removal in a short-term enhanced weathering study. Front. Clim. 6, 1524998. doi: 10.3389/fclim.2024.1524998

ten Berge, H. F. M., van der Meer, H. G., Steenhuizen, J. W., Goedhart, P. W., Knops, P., and Verhagen, J. (2012). Olivine weathering in soil, and its effects on growth and nutrient uptake in ryegrass (Lolium perenne L.): a pot experiment. PLoS One 7, e42098. doi: 10.1371/journal.pone.0042098

Vienne, A., Poblador, S., Portillo-Estrada, M., Hartmann, J., Ijiehon, S., Wade, P., et al. (2022). Enhanced weathering using basalt rock powder: carbon sequestration, co-benefits and risks in a mesocosm study with Solanum tuberosum. Front. Clim. 4, 869456. doi: 10.3389/fclim.2022.869456

Vienne, A., Cox, T., Niron, H., Guenet, B., Poetra, R., Steinwidder, L., et al. (2026). Integrating experiments and models to unravel interactions between soil organic matter and enhanced weathering. Environ. Sci. Technol. 60, 19249–19261. doi: 10.1021/acs.est.6c00236

13 Tables

Table 1. Physicochemical properties of the 29 natural, agricultural and engineered technosol soils used in the GH2025 mesocosm experiment. Exchangeable-cation detail is given in Supplementary Table S1.

Soil	Code	pH	CEC_{eff} (cmol kg^{-1})	KA5 classification (DE)	USDA classification	Sand (%)	Silt (%)	Clay (%)	Total N (%)	Total C (%)	Inorg. C (%)	Org. C (%)	LOI 550 (%)	EC (µS cm^{-1})
Alkener Berg	ALK	6.48	11.59	silty loam	silt loam	22.7	52.30	25.00	0.118	1.193	b.d.	1.193	4.47	132
Am Langen Stein	AML	7.28	21.58	medium silty clay	silty clay loam	17.3	51.30	31.40	0.192	1.935	b.d.	1.935	6.15	115
Ballirankin	BAL	6.07	12.34	strongly sandy loam	sandy loam	61.9	20.60	17.50	0.287	3.442	0.010	3.432	8.35	157
Danskenfeld	DAN	5.57	4.23	medium loamy sand	sandy loam	78.5	12.80	8.70	0.103	1.213	b.d.	1.213	3.00	56
Fabrikfeld	FAB	7.50	25.35	silty loam	silt loam	26.4	54.60	19.00	0.274	11.393	6.795	4.598	8.61	204
Flughafen	FLU	6.65	9.78	slightly clayey loam	clay loam	37.0	33.10	29.90	0.157	1.556	0.109	1.448	5.66	74
Gartenacker	GAR	5.67	7.35	slightly loamy sand	sandy loam	77.4	11.70	10.90	0.087	0.921	b.d.	0.921	2.91	116
Griffelsberg	GRI	6.44	9.51	strongly loamy sand	sandy loam	61.3	23.70	15.00	0.126	1.423	0.116	1.307	3.74	122
Hopfen	HOP	5.35	8.08	strongly loamy sand	sandy loam	65.3	21.20	13.50	0.166	1.621	b.d.	1.621	4.76	94
Im Boden	IMB	6.26	13.60	silty loam	silt loam	17.8	55.50	26.70	0.197	1.838	0.104	1.734	6.08	182
Kaltenelse	KAL	6.76	18.98	medium silty clay	silty clay loam	9.5	53.60	37.00	0.171	1.656	b.d.	1.656	6.35	96
Kirchweg	KIR	5.86	9.33	strongly loamy sand	sandy loam	69.0	15.20	15.80	0.102	1.104	b.d.	1.104	3.61	76
Luessteile	LUS	7.20	19.34	strongly sandy loam	sandy clay loam	60.5	17.40	22.10	0.204	2.124	0.250	1.874	6.51	201
LUFA 2.2 C	LUF	5.51	9.42	strongly sandy loam	sandy loam	67.2	15.40	17.40	0.237	2.551	b.d.	2.551	6.61	120
Marburg	MAR	5.47	9.53	strongly silty clay	silt loam	9.0	65.20	25.90	0.130	1.200	0.040	1.160	4.48	73
Marsianer	MIR	6.50	1.13	slightly clayey sand	loamy sand	84.3	2.60	13.10	n.d.	0.058	b.d.	0.058	1.23	5
Marsianer BBS	MBS	6.39	n.d.	slightly clayey sand	loamy sand	n.d.	n.d.	n.d.	0.138	2.109	b.d.	2.109	n.d.	13
Melm Wald	MEL	6.88	13.89	silty loam	silt loam	9.4	63.90	26.70	0.127	1.210	b.d.	1.210	4.44	83
Pod 12	POD	3.68	2.70	sand	sand	90.5	4.70	4.80	0.030	1.136	b.d.	1.136	2.85	20
Pod 12 BBS	PBS	3.80	n.d.	slightly clayey sand	loamy sand	n.d.	n.d.	n.d.	0.195	3.261	b.d.	3.261	n.d.	35
Pod 12 MIR	PIR	4.08	1.99	slightly clayey sand	sandy loam	79.7	4.90	15.40	0.017	0.749	b.d.	0.749	2.53	8
Pruem	PRU	5.28	11.26	slightly clayey loam	clay loam	32.3	36.90	30.70	0.310	2.714	b.d.	2.714	8.94	178
Radweg	RAD	5.67	9.04	slightly clayey loam	clay loam	23.6	44.00	32.50	0.191	1.686	b.d.	1.686	6.02	82
Ramsgrange	RAM	5.80	12.03	slightly clayey loam	clay loam	35.7	35.00	29.30	0.223	2.375	b.d.	2.375	6.81	73
Rastlinstatt	RAS	5.82	9.99	slightly clayey loam	loam	43.7	30.70	25.70	0.155	1.622	0.108	1.514	5.52	67
Schlehbach Kreuz	SBK	7.19	17.70	slightly sandy loam	loam	33.6	44.70	21.80	0.185	2.463	0.636	1.827	5.49	191
Streugarten	STR	6.69	16.77	medium silty clay	silty clay loam	9.5	54.10	36.40	0.178	1.694	b.d.	1.694	6.11	98
Westerwald	WES	6.26	9.97	slightly clayey loam	silty clay loam	19.3	46.20	34.50	0.189	1.530	b.d.	1.530	6.25	88
Wolfland	WOL	3.34	7.91	slightly clayey sand	sand	91.8	3.10	5.20	0.019	0.720	b.d.	0.720	1.83	443

KA5 = German soil-texture class after the Bodenkundliche Kartieranleitung, 5th edn (Ad-hoc-AG Boden, 2005); class boundaries differ from the USDA textural scheme.

BBS = Black Bavarian Swamp, an organic-rich material blended with Pod 12 and Marsianer to increase organic carbon content, creating the technosols Pod 12 BBS and Marsianer BBS.
n.d. = not determined.
b.d. = below the analytical detection limit (see Supplementary Table S5 for detection limits).

Table 2. Quantitative mineralogical composition (XRD, wt%) of the CDR-relevant feedstock phases in the 19 feedstocks used in GH2025. Feedstocks are grouped into seven categories ordered from highest to lowest expected reactivity. Analytical detection limits are given in Supplementary Table S5, and complete quantitative mineralogical compositions are provided in Supplementary Table S7.

Mineral	Industrial	Carbonates		Carbonate–silicate mixes			Ca-(Mg-)silicates				Ultramafic silicates		Mafic silicates					Felsic silicates	
	Steel slag	BB limestone	MK limestone	Angryd Frankenstein	Metabasalt	MK + VV	Calcio-olivine	Monticellite	Monticellite skarn	Wollastonite skarn	Peridotite	VV peridotite	Eifelgold basanite	BD nephelinite	DP basalt	KL nephelinite	TC nephelinite	Glacial power flour	Glacial rock flour
Oxides / hydroxides																			
Portlandite	19.5	–	–	–	–	–	–	–	–	–	–	–	–	–	–	–	–	–	–
Periclase	0.7	–	–	2.4	–	–	22.2	12.5	–	–	–	–	–	–	–	–	–	–	–
Perovskite	–	–	–	–	–	–	–	–	6.1	–	–	–	–	0.8	–	–	–	–	–
Srebrodolskite	17.8	–	–	–	–	–	–	–	–	–	–	–	–	–	–	–	–	–	–
Carbonates																			
Calcite	8.3	97.6	85.0	10.5	27.2	42.7	0.9	–	–	1.5	–	0.4	–	–	0.6	–	–	–	0.6
Dolomite/Ankerite	–	2.0	14.6	1.9	–	7.3	–	–	–	–	–	–	–	–	–	–	–	0.6	0.5
Silicates																			
K-feldspar	–	–	–	–	10.1	–	–	–	0.8	–	–	–	–	–	–	3.8	–	6.8	6.6
Plagioclase	–	–	–	7.3	15.5	–	–	–	2.5	–	–	–	7.7	–	44.4	11.0	10.8	35.0	35.3
Clinopyroxene	–	–	–	9.1	1.8	0.8	–	0.3	–	7.5	1.6	1.7	49.4	58.4	26.5	36.4	42.1	0.8	0.8
Orthopyroxene	–	–	–	–	–	9.3	–	–	–	–	5.0	18.6	–	–	–	–	–	–	–
Amphibole	–	–	–	–	–	–	–	–	1.1	–	1.9	–	–	–	–	–	–	14.3	14.1
Olivine	–	–	–	10.3	3.6	35.8	–	7.9	–	–	79.2	71.5	11.2	3.4	–	9.3	12.7	–	–
Monticellite	–	–	–	8.3	–	–	1.2	51.0	24.3	–	–	–	–	–	–	–	–	–	–
Nepheline	–	–	–	6.3	–	–	–	–	–	–	–	–	9.3	22.3	–	18.7	18.6	–	–
Leucite	–	–	–	1.7	–	–	–	–	–	–	0.3	–	12.6	–	–	1.9	–	–	–
Analcime	–	–	–	1.6	–	–	–	–	–	–	–	–	1.3	–	–	5.0	3.2	–	–
C2S* (α+α'+β+γ)	29.9	–	–	6.0	–	–	33.3	–	–	1.6	–	–	–	–	–	–	–	–	–
Wollastonite	–	–	–	–	–	–	1.3	–	8.3	85.6	–	–	–	–	–	–	–	–	–
Merwinite	–	–	–	2.9	–	–	19.6	22.7	–	–	–	–	–	–	–	–	–	–	–
Bredigite	–	–	–	2.2	–	–	13.6	–	–	–	–	–	–	–	–	–	–	–	–
Melilite group	–	–	–	1.0	–	–	0.8	–	13.3	–	–	–	–	1.8	–	–	–	–	–
Pectolite	–	–	–	–	–	–	–	–	3.3	–	–	–	–	–	–	–	–	–	–
2:1 layer silicates	–	–	–	16.8	6.2	–	–	–	7.1	–	0.5	–	1.8	1.2	22.6	5.4	2.3	33.1	28.5
Chlorite	–	–	–	–	22.5	–	–	–	1.8	–	1.4	–	–	–	–	–	–	0.6	1.4
Garnet	4.5	–	–	0.9	–	–	–	–	11.0	–	–	–	–	–	–	–	–	–	–
Serpentine	–	–	–	4.0	–	3.3	–	–	–	–	10.3	6.6	–	–	–	–	–	–	–
Phosphates																			
Apatite	–	–	–	1.3	0.8	–	–	–	–	–	–	–	1.2	2.6	–	2.4	2.8	–	–

All values are weight per cent (wt %).

– = not detected.

* Four dicalcium-silicate polymorphs, C2S, are combined into one row. The complete quantitative XRD composition is given in Supplementary Table S7

Table 3. Feedstock particle size distributions determined by wet laser diffraction and BET specific surface areas of the GH2025 feedstocks, including original 'as-received' (O) and milled (M) grain-size variants. Complete particle size distributions are provided in Supplementary Table S8.

Feedstock category	Sample	BET ($m^2 g^{-1}$)	d_{10} (µm)	d_{50} (µm)	d_{90} (µm)	Span
Industrial	Steel slag O	13.3	6.1	76.4	167.2	2.1
Carbonates	BB limestone O	0.7	6.6	137.9	354.7	2.5
	BB limestone M	1.1	2.7	9.0	28.7	2.9
	MK limestone O	0.9	6.9	147.8	279.7	1.8
	MK limestone M	1.4	2.5	9.1	25.5	2.5
Carbonate–silicate mixes	Angryd Frankenstein O	16.5	0.9	2.0	3.9	1.5
	Metabasalt O	2.6	2.4	11.2	41.2	3.5
	MK + VV M	2.0	3.0	14.3	38.3	2.5
Ca-(Mg-)silicates	Calcio-olivine M	1.1	3.5	8.2	15.4	1.4
	Monticellite O	0.1	107.5	213.0	372.6	1.2
	Monticellite M	0.6	5.2	19.5	44.5	2.0
	Monticellite skarn M	3.9	0.7	5.3	12.9	2.3
	Wollastonite skarn O	1.3	2.2	13.4	32.6	2.3
Ultramafic silicates	Peridotite O	1.9	4.1	19.6	50.6	2.4
	VV peridotite O	2.0	25.9	105.0	223.1	1.9
	VV peridotite M	2.7	4.2	22.6	45.7	1.8
Mafic silicates	Eifelgold basanite O	2.3	3.9	38.5	447.5	11.5
	BD nephelinite O	9.8	7.7	54.5	232.6	4.1
	BD nephelinite M	7.2	3.2	12.7	29.9	2.1
	DP basalt O	1.0	0.8	6.3	448.7	71.0
	DP basalt M	9.1	2.1	9.1	21.0	2.1
	KL nephelinite O	19.2	2.2	10.3	26.9	2.4
	KL nephelinite M	17.1	1.7	7.8	20.6	2.4
	TC nephelinite M	11.9	3.4	11.8	26.9	2.0
Felsic silicates	Glacial power flour O	16.4	0.8	2.4	5.2	1.8
	Glacial rock flour O	17.8	0.4	1.6	3.8	2.1

O = original 'as-received' grain size; M = milled to approximately < 70 µm before application.

BET values <0.5 $m^2 g^{-1}$ fall below the validated quantification range and are reported as indicative only.

Supplementary Material

1 Extended experimental setup

1.1 Lysimeter construction

The core experimental setup, originally developed for GH2023, is described in detail in Hammes et al. (2025), with the key information relevant to the present study summarised below.

Each mesocosm consists of a stacked pair of 10 L lysimeter buckets (diameter ≈ 25.6 cm, height 26.3 cm), forming a soil-column system above a leachate collection tank (Figure 1). The upper bucket contains the soil column, feedstock amendment and vegetation, while the lower bucket functions as the leachate collection reservoir. The lower bucket is fitted with two push-in connectors linked by a transparent LDPE tube, which was used to monitor the standing leachate level and to drain samples during collection. The upper bucket was placed on the perforated lid of the lower bucket and a Nitrile O-ring sealed the headspace of the leachate bucket airtight. Its base is lined with polypropylene root fleece and a 3 cm layer of washed quartz sand to promote even drainage and reduce transport of fine material into the collection tank. Twenty average sized earthworms, consisting of a mixed inoculum of *Eisenia foetida*, *Dendrobaena veneta* and *Lumbricus terrestris*, were added to each pot to promote bioturbation. In selected mesocosms, 5 g feedstock ‘tea-bag’ sachets were buried to monitor changes in feedstock mass, surface area and mineralogy over time (cf. Hammes et al., 2025).

Three modifications were introduced in GH2025. First, the drainage interface between the soil bucket and collection tank was improved by enlarging and aligning the perforations in the bucket base and tank lid, reducing the risk of clogging by fine particulates and improving drainage consistency across the mesocosm array. Second, feedstock equivalent to 40 t ha-1 was mixed throughout the full ~20 cm soil column, rather than being confined to an upper 15 cm amended layer above 10 cm of unamended soil as in GH2023. This removed an artificial discontinuity within the soil profile, increased the soil–feedstock contact volume and better approximates a field-scale tillage. Third, the single-species Lolium perenne cover used in GH2023 was replaced with a grass–legume mixture comprising by seed mass: 40% Festuca arundinacea, 30% Lolium perenne subsp. perenne and 30% Trifolium repens 'Microclover'. The seed mixture was selected to incorporate contrasting rooting depths and root-derived organic-acid exudation, which may promote feedstock weathering while supporting vegetation establishment across soils differing in pH, texture and nutrient status. In strongly acidic soils and technosols, the seed mixture was supplemented with the acid-tolerant bentgrasses Agrostis capillaris and Agrostis canina (0.25 g pot-1 each). The full rationale for the vegetation change, and its potential effects on rhizosphere weathering are described in Supplementary Section S1.3.

1.2 Greenhouse operation

Compared with outside ambient temperatures, the greenhouse was consistently warmer and had lower relative humidity, with the largest differences observed in winter, when the greenhouse was heated. Daily mean air temperature was typically 18–30 °C (median ~21–22 °C) and relative humidity 35–70% (median ~50–55%), compared with medians of approximately 10 °C and 80% outside. Automated drip irrigation is supplied from a rainwater cistern using Netafim NetBow rings. Irrigation is delivered at six-hour intervals, with a

baseline rate of approximately 2,000 mm yr^{-1}, increasing to as much as 4,000 mm yr^{-1} during periods of high evapotranspiration to maintain leachate generation.

Pest and disease pressure was managed through an integrated biological-control programme rather than with synthetic pesticides. The composition and volume of milk sprays applied against powdery mildew were recorded to account for their potential contribution to leachate ion chemistry. Further details of the control agents are provided in Supplementary Section S1.4 and Supplementary Table S10.

1.3 Vegetation

In GH2023, poor establishment of the single-species *Lolium perenne* vegetation on some soils required re-seeding and vegetation management which disturbed the soil surface and affected leachate chemistry. A three-species grass–legume mixture (by seed mass: 40% *Festuca arundinacea*, 30% *Lolium perenne* subsp. *perenne* (tetraploid), 30% *Trifolium repens* 'Microclover') was therefore chosen to improve and equalise vegetation establishment across soils spanning extreme differences in pH, texture and nutrient status.

The mixture was selected for complementary rooting depth and root-derived organic-acid exudation rather than biomass yield, as vascular plants accelerate silicate weathering through elevated rhizosphere pCO_2, proton release and exudation of cation-complexing organic acids that promote mineral dissolution (Drever, 1994; Cochran & Berner, 1993; Olsen & Rimstidt, 2008). *F. arundinacea* contributes a deep, stress-tolerant root system, *L. perenne* establishes rapid ground cover, and *T. repens* lowers rhizosphere pH and supplies nitrogen via N_2 fixation (McNeill & Wood, 1990), with a low-fixing microclover cultivar chosen to avoid excess soil nitrogen suppressing organic-acid exudation by the grasses.

On the most strongly acidic soils and technosols, where the three-species mixture established poorly, two acid-tolerant bentgrasses, *Agrostis capillaris* and *Agrostis canina* (0.25 g pot^{-1} each), were added. These calcifuge pioneer grasses have well-documented ecotypic tolerance of acidic soils (Gartside & McNeilly, 1974), and were included to ensure comparable ground cover and root activity across the full soil pH range.

1.4 Pest and disease control

Pest and disease pressure was managed with an integrated biological-control programme rather than synthetic pesticides, fungicides or acaricides to avoid introducing ions that would interfere with the leachate ion balance. Aphids (Aphididae), glasshouse whitefly (*Trialeurodes vaporariorum*), thrips (Thysanoptera), spider mites (Tetranychidae) and fungus gnats (Sciaridae) were all observed during the trial and controlled with commercially reared beneficials, including predatory mites (Phytoseiidae e.g., *Amblyseius spp.*, *Neoseiulus spp.*), parasitoid wasps (e.g., *Encarsia formosa*, *Aphidius spp.*), predatory beetles (Coccinellidae e.g., *Adalia bipunctata*) and lacewings (Chrysopidae, e.g., *Chrysoperla carnea*), and entomopathogenic nematodes (e.g., *Steinernema spp.*, *Heterorhabditis spp.*). These biological agents were applied as individual organisms, as egg cards, or in small quantities of inert carrier and substrate material, with repeated applications made in response to observed pest pressure. Yellow sticky traps were used for pest monitoring only, in winter when no beneficials were present. Beneficials were supplied by GrünTeam Garten-Shop / Michael Hoß GmbH (Penzberg, Germany). The target organisms, the specific biological agents used against each and their form of application are listed in Supplementary Table S10.

Powdery mildew was treated with foliar applications of raw (unpasteurised) cow's milk diluted with irrigation water 1:4 or 1:5 (milk:water, v/v), depending on infection severity. . Raw milk is used because its naturally occurring microbial community contributes to the antifungal effect (Bettiol, 1999). Applications are logged for each pot, and the associated Ca, Mg, Na and K inputs are included in the pot-level ion balance to distinguish them from weathering-derived cations in the leachate record.

Fifteen flowering strips were established within the greenhouse as habitat for the beneficials. Plant species were selected to provide staggered flowering so that nectar and pollen are available continuously through the season. The species were selected for their low growth height and avoidance of wind-dispersed seeds that could contaminate the mesocosms.

2 Soil preparation, homogenisation and archiving

Before mesocosm assembly, each soil was prepared from a single large bulk sample. Pebbles and root fragments were removed using a rotating drum sieve, after which the remaining soil was repeatedly mixed until homogeneous. The mesocosms were then filled with equal volumes of the homogenised soil. During filling, sub-samples were collected from spatially distributed points within each soil column and combined to yield one archived composite baseline sample per pot (n = 450). The baseline samples were air-dried and archived for subsequent analyses. Sub-samples designated for laboratory analysis were then dried at 40 °C and passed through a 2 mm sieve. As a baseline sample is available for every individual pot, changes in soil composition can be evaluated relative to the corresponding pot-level baseline, rather than against a mean baseline for each soil.

3 Detailed leachate and soil analytical protocols

The analytical methods summarised in Table S5 are described in further detail below. Unless otherwise stated, all protocols follow those described by Hammes et al. (2025).

3.1 Leachate sampling

Leachate water samples were collected at intervals of approximately 6 to 8 weeks. Before sample collection, each borosilicate measuring cylinder and Erlenmeyer flask was rinsed with an initial aliquot of the leachate, which was then discarded. The discarded rinse volume was included in the total leachate volume recorded for each sampling event.

3.2 Total alkalinity

For every mesocosm, total alkalinity (TA) was determined on a 100 ml leachate aliquot using a HACH Digital Titrator (Model 16900 (RSD ± 1 %)). Bromocresol Green–Methyl Red indicator powder was added, and the sample titrated dropwise with 1.6 N or 0.16 N sulfuric acid until the colour changed from green to red at the endpoint at pH 4.3. Following the HACH method, acid consumption was initially expressed as mg l^{-1} $CaCO_3$. This value is converted to mg l^{-1} HCO_3^- by using a factor of 1.22, divided by the molar mass of HCO_3^- (61 g mol^{-1}) and multiplied by 1000 to obtain micromoles (µmol(eq) l^{-1}). Although bicarbonate is expected to dominate, the measurement can also include contributions from other proton-accepting species, and thus is reported as total alkalinity.

3.3 In situ pH, electrical conductivity, dissolved oxygen and temperature

Leachate pH, electrical conductivity (EC), dissolved oxygen concentration and oxygen saturation were measured immediately after sampling. 200 ml of leachate was transferred into a pre-rinsed measuring cylinder and analysed using a portable WTW multi-parameter instrument (MultiLine® Multi 3630 IDS) equipped with a Sentix® 940-x pH sensor (SD ± 0.1 pH unit), a TetraCon® 925 EC sensor (SD ± 5 µS cm^{-1}), and an FDO® 925 optical IDS dissolved oxygen sensor (SD ± 0.2 mg l^{-1} for dissolved O_2 concentration, and ± 2% O_2 saturation). Leachate temperature was recorded as the mean reading from the three integrated temperature sensors.

3.4 Dissolved inorganic carbon, cations and anions

On a small subset of leachate samples, filtered cation samples were acidified and analysed by ICP-OES at Analytik Institut Rietzler GmbH, Fürth, Germany, while filtered unacidified anion samples were analysed by ion chromatography to constrain charge balance and to assess whether changes in EC and alkalinity reflect weathering-derived base cation release, carbonate alkalinity export, or the mobilisation of non-alkalinity ions.

Dissolved inorganic carbon was determined on filtered samples (<0.45 µm) using a Shimadzu TOC-L CPH analyser with an ASI-L autosampler (Shimadzu, Japan), following acidification with phosphoric acid and quantification of the released CO_2 by non-dispersive infrared (NDIR) detection.

4 Carbonate-corrected theoretical maximum CDR potential

4.1 Theoretical maximum CDR potential of a feedstock (E_{pot})

The theoretical maximum CDR potential of a feedstock (E_{pot}, in kg CO_2 per tonne of feedstock) can be estimated from its bulk elemental composition, expressed as major-element oxides, using the mass-balance approach of Renforth (2019), modified after the Steinour (1959) formula. This calculation assumes complete feedstock dissolution, and that all base cations are charge balanced by bicarbonate generated via carbonic-acid weathering, regardless of dissolution rate or timescale. It does not account for cations hosted within carbonate minerals, whose dissolution produces two moles of bicarbonate but captures only one mole of new CO_2, as the second mole of carbon is supplied by the carbonate mineral itself. E_{pot} is therefore an upper-bound CDR estimate.

$$E_{pot} = \frac{M_{CO_2}}{100}\left(\alpha\frac{CaO}{M_{CaO}} + \beta\frac{MgO}{M_{MgO}} + \varepsilon\frac{Na_2O}{M_{Na_2O}} + \theta\frac{K_2O}{M_{K_2O}} + \gamma\frac{SO_3}{M_{SO_3}} + \delta\frac{P_2O_5}{M_{P_2O_5}}\right)\cdot 10^3 \cdot \eta$$

Oxide concentrations are expressed in wt %, molar masses (M_i) are denoted in g mol^{-1}, and coefficients α, β, γ, δ, ε, and θ represent the stoichiometric contribution of each oxide. At pH < 10, α = β = ε = θ = 1. Acid-forming oxides (SO_3, P_2O_5) consume alkalinity and thus γ and δ are negative values (Renforth, 2019). The parameter η is the molar ratio of CO_2 sequestered to divalent cation released, and was set to 2 to represent the theoretical maximum CDR assuming carbonic-acid weathering with no downstream losses. The factor 10^3 converts the result to kg CO_2 t^{-1}.

The coefficient δ for P_2O_5 varies with soil water pH, from -1.06 for pH < 6, -1.39 at pH 7, -1.86 at pH 8 and -2 for pH > 9. As the majority of soils used in our GH2025 experiment have a soil pH below 7, a δ-value of -1 was adopted. Even for the higher-pH soils, this only results in a maximum overestimation of 1.2 % which we deem negligible.

The sulfate term was omitted because SO_3 was not measured, and XRD indicated negligible S-bearing mineral abundance. For the two feedstocks containing detectable S-bearing phases, 2.7 wt% haüyne in the BD nephelinite and 1 wt% ye'elimite in the calcio-olivine, the estimated correction in E_{pot} was only -4.2 and -1.4 kg CO_2 t^{-1}, respectively, which is below the propagated uncertainty of the quantitative XRD analysis.

Using the above parameter values, the E_{pot} was calculated for each of 19 feedstocks using the following simplified equation:

$$E_{pot} = \frac{M_{CO_2}}{100}\left(\frac{CaO}{M_{CaO}} + \frac{MgO}{M_{MgO}} + \frac{Na_2O}{M_{Na_2O}} + \frac{K_2O}{M_{K_2O}} - \frac{P_2O_5}{M_{P_2O_5}}\right) \cdot 10^3 \cdot 2$$

4.2 Carbonate-corrected theoretical maximum CDR potential (Max CDR_{pot})

Whole-rock CDR potential calculations cannot distinguish between cations held in silicate or carbonate phases, and may therefore overestimate CDR potential when carbonate minerals are present (Power et al., 2025). We therefore used quantitative XRD to estimate the proportion of CaO and MgO hosted in calcite and dolomite, and based on their stoichiometry, discounted their contributions to E_{pot} by 50 %. We refer to this carbonate-corrected value as Max CDR_{pot}. This correction is most significant for carbonate-rich materials such as limestone, but may also be non-negligible for silicate feedstocks containing accessory calcite or dolomite. The carbonate-hosted oxide fraction were calculated as follows:

Conversion of carbonate phases to oxide equivalents

Equivalent CaO and MgO concentrations were calculated from the quantitative XRD abundance of each carbonate phase according to its mineral stoichiometry, using the ratio of the molar mass of the relevant oxide to that of the mineral, for example:

$$CaO_{calcite} = Calcite\,(wt\%) \cdot \frac{M_{CaO}}{M_{CaCO_3}}$$

$$CaO_{dolomite} = Dolomite\,(wt\%) \cdot \frac{M_{CaO}}{M_{CaMg(CO_3)_2}}$$

$$MgO_{dolomite} = Dolomite\,(wt\%) \cdot \frac{M_{MgO}}{M_{CaMg(CO_3)_2}}$$

where M(i) denotes molar mass in g mol^{-1}, and all mineral and oxide concentrations are expressed in wt%.

Calculation of carbonate-corrected oxide concentrations

For the calcite and dolomite identified in our feedstocks, the carbonate-hosted CaO and MgO contributions were reduced by 50 %:

$$CaO_{corr} = CaO_{XRF} - \frac{1}{2}\,CaO_{calcite} - \frac{1}{2}\,CaO_{dolomite}$$

$$MgO_{corr} = MgO_{XRF} - \frac{1}{2}\,MgO_{dolomite}$$

Calculation of Max CDR_{pot}

The carbonate-corrected theoretical maximum CDR potential (Max CDR_{pot}) was calculated by substituting the corrected CaO and MgO concentrations into the modified Renforth (2019) equation:

$$Max\ CDR_{pot} = \frac{M_{CO_2}}{100}\left(\frac{CaO_{corr}}{M_{CaO}} + \frac{MgO_{corr}}{M_{MgO}} + \frac{Na_2O}{M_{Na_2O}} + \frac{K_2O}{M_{K_2O}} - \frac{P_2O_5}{M_{P_2O_5}}\right) \cdot 10^3 \cdot 2$$

Both E_{pot} and Max CDR_{pot} are presented in Table S6. Uncertainty in the XRF and XRD inputs was not propagated. The correction is negligible for carbonate-free feedstocks, but approaches 50 % for carbonate-dominated limestones, e.g., for MK limestone, Max CDR_{pot} is roughly half of E_{pot} (431 vs 874 kg CO_2 t^{-1}); for metabasalt, a silicate with ~27 wt% calcite, the reduction is smaller (288 vs 408 kg CO_2 t^{-1}); and for the carbonate-free silicate Peridotite, the two values are identical (1037 kg CO_2 t^{-1}).

5 Supplementary tables (separate table)

The supplementary data can be found at Github: https://github.com/dirkpaessler/carbdown_greenhouse_experiment_2025 and archived for citation via Zenodo: doi.org/10.5281/zenodo.23798190.

Supplementary Table S1. Soil CEC and exchangeable cation concentrations of the agricultural soils and engineered technosols used in GH2025. T-value = effective CEC (sum of exchangeable cations); S-value = sum of exchangeable base cations (Ca, Mg, K, Na); H-value = exchangeable acidity.

Supplementary Table S2. Soil geochemistry and loss on ignition (LOI) of the agricultural soils and engineered technosols used in GH2025. Major-element oxide concentrations were determined by XRF. LOI was measured after heating for 2 h at 1000 °C. Total represents the sum of the major-element oxides plus LOI. Analytical detection limits are given in Supplementary Table S5.

Supplementary Table S3. Quantitative mineralogical composition of the agricultural soils and engineered technosols used in GH2025, as determined by XRD. Values are in wt%. Analytical detection limits are given in Supplementary Table S5.

Supplementary Table S4. Particle size distribution of the agricultural soils and engineered technosols used in GH2025, as determined by wet sieving and SediGraph analysis. Values include the sand, silt and clay fractions and full grain-size distribution.

Supplementary Table S5. Analytical methods used for the initial characterisation of the 29 soils and 19 feedstocks and for leachate monitoring during GH2025. Further methodological details are provided in Hammes et al. (2025) and Supplementary Section S3.

Supplementary Table S6. Bulk major-element oxide and selected trace-element compositions, loss on ignition (LOI) and theoretical maximum CDR potentials of the 19 feedstocks used in GH2025. Major-element oxide and trace-element concentrations were determined by XRF. LOI was measured after heating for 2 h at 1000 °C. Total represents the sum of the major-element oxides plus LOI. Analytical detection limits are given in Supplementary Table S5. E_{pot} and Max CDR_{pot} are defined in Supplementary Section S4.

Supplementary Table S7. Quantitative mineralogical composition (wt%) of the 19 feedstocks used in GH2025, as determined by XRD. Feedstocks are grouped in seven categories according to their dominant ERW-relevant mineralogy, with categories ordered from highest to lowest expected reactivity. C2S = dicalcium silicate; C3S = tricalcium silicate.

Supplementary Table S8. Particle size distributions of the GH2025 feedstocks, including original ‘as-received’ and milled grain-size variants, as determined by wet laser diffraction.

Supplementary Table S9. Overview of soil and feedstock combinations for the GH2025 experiment. All pots were sown with the GH2025 grass–legume mixture, except 13 LUFA 2.2 C pots in the bridge experiment, which were only sown with the GH2023 *Lolium perenne* monoculture.

Supplementary Table S10. Pest and disease control measures used in GH2025. Further details are provided in Supplementary Section S1.4.

6 Supplementary references

Bettiol, W. (1999). Effectiveness of cow’s milk against zucchini squash powdery mildew (*Sphaerotheca fuliginea*) in greenhouse conditions. *Crop Prot.* 18, 489–492. doi: 10.1016/S0261-2194(99)00046-0

Cochran, M. F., and Berner, R. A. (1993). Enhancement of silicate weathering rates by vascular land plants: quantifying the effect. Chem. Geol. 107, 323–326. doi: 10.1016/0009-2541(93)90176-J

Drever, J. I. (1994). The effect of land plants on weathering rates of silicate minerals. Geochim. Cosmochim. Acta 58, 2325–2332. doi: 10.1016/0016-7037(94)90013-2

Gartside, D. W., and McNeilly, T. (1974). The potential for evolution of heavy metal tolerance in plants. II. Copper tolerance in normal populations of different plant species. Heredity 32, 335–348. doi: 10.1038/hdy.1974.40

Hammes, J. S., Hartmann, J., Barth, J. A. C., Linke, T., Smet, I., Hagens, M., et al. (2025). Soil processes govern alkalinity and cation retention in enhanced weathering for carbon dioxide removal. EGUsphere [preprint]. doi: 10.5194/egusphere-2025-5402

McNeill, A. M., and Wood, M. (1990). Fixation and transfer of nitrogen by white clover to ryegrass. Soil Use Manag. 6, 84–86. doi: 10.1111/j.1475-2743.1990.tb00810.x

Olsen, A. A., and Rimstidt, J. D. (2008). Oxalate-promoted forsterite dissolution at low pH. Geochim. Cosmochim. Acta 72, 1758–1766. doi: 10.1016/j.gca.2007.12.026

Power, I.M., Hatten, V.N.J., Guo, M., Schaffer, Z.R., Rausis, K., and Klyn-Hesselink, H. (2025). Are enhanced rock weathering rates overestimated? A few geochemical and mineralogical pitfalls. Frontiers in Climate 6:1510747. doi: 10.3389/fclim.2024.1510747

Renforth, P. (2019). The negative emission potential of alkaline materials. *Nature Communications* 10, 1401. doi: 10.1038/s41467-019-09475-5

Steinour, H.H. (1959). Some effects of carbon dioxide on mortars and concrete – discussion. *Journal of the American Concrete Institute* 30, 905–907.